Journal of Modern Energy Research
Vol. 8, Jun 2026, pp. 11–16
ISSN: 3078-3534, DOI: 10.56947/jmer.v8.3

Thermal-Electrical Co-Optimization of Liquid Hydrogen-Cooled Superconducting Motors for Heavy-Duty Transport

Rajesh Kumar[1], Sunita Devi[2], Mohammed Saif[3]

[1]Department of Electrical Engineering, Savitribai Phule Pune University, Pune, India
[2]Department of Electrical and Computer Engineering, Lovely Professional University, Phagwara, India
[3]Department of Power Engineering, Prince Mohammad Bin Fahd University, Al Khobar, Saudi Arabia

Article Info

Article history:
Received Feb 12, 2026
Revised Mar 22, 2026
Accepted Apr 12, 2026

Keywords:
high-temperature superconductivity, liquid hydrogen, cryogenic cooling, electric propulsion, fuel cell

ABSTRACT

Full electrification of heavy-duty transport is constrained by the low specific power density of conventional electric drives, and High-Temperature Superconducting (HTS) machines, while capable in principle of meeting aviation power-density targets above 15 kW/kg, are normally negated by the mass of active cryocoolers. We introduce an integrated cryogenic-electric machine architecture in which liquid hydrogen (LH_2) serves a dual role, first as a direct cryo-coolant for an HTS synchronous motor and subsequently as fuel for a proton exchange membrane fuel cell stack. Coupled finite-element electromagnetic and transient computational fluid dynamics simulation of a 2 MW aircraft propulsion motor shows that the LH_2 flow demanded by the fuel cell exceeds the motor's cooling requirement across all flight phases, eliminating dedicated cryocooling mass and yielding a system-level power density of 27.8 kW/kg.

Corresponding Author:
Rajesh Kumar
Department of Electrical Engineering
Savitribai Phule Pune University
Pune, India
Email: rajesh.kumar@unipune.ac.in

1. INTRODUCTION

Net-zero aviation targets for 2050 require commercial narrow-body aircraft to adopt electric propulsion systems with specific power densities exceeding 15 kW/kg. Conventional electric machines are constrained by the magnetic saturation of iron cores and the ohmic heating of copper windings, and asymptotically plateau at around 5–8 kW/kg [1]. High-temperature superconductors such as yttrium barium copper oxide (YBCO) can sustain current densities roughly two orders of magnitude greater than copper with zero DC resistance, offering a path past this ceiling [2, 3]. Realizing this potential requires maintaining the superconductor at cryogenic temperatures, typically 20–50 K, and the mass of conventional active cryocoolers has historically negated the power-density advantage that HTS windings otherwise provide [4].

The aviation industry is simultaneously moving toward liquid hydrogen as a primary energy carrier, stored on board at approximately 20 K and consumed either through combustion or, increasingly, through proton exchange membrane (PEM) fuel cells [5–7]. This coincidence of cryogenic requirements motivates the present work: rather than treating HTS cooling and hydrogen fuel supply as separate subsystems, we route the cryogenic sensible and latent heat of the LH_2 stream through the HTS motor before the hydrogen is vaporized, warmed, and delivered to the fuel cell stack [8, 9]. Recent demonstrator and design studies of fully and partially superconducting aircraft motors in the 100 kW to multi-megawatt range confirm the electromagnetic feasibility of this class of machine [10–12], and progress in thermal management of both HT-PEM fuel cells [13, 14] and cryogenic heat exchangers [9] increasingly supports the system-level integration proposed here. This paper develops and numerically evaluates that integrated architecture for a 2 MW aircraft propulsion motor, quantifying the thermal margin between fuel-driven LH_2 flow and motor cooling demand across a representative flight profile. The multiphase computational fluid dynamics of the LH_2 stream solved here is, at the governing-equation level, an instance of the incompressible Navier–Stokes system with wall friction; see Zongo and Kyelem for a treatment of the three-dimensional Navier–Stokes equation with multivalued friction in a purely mathematical setting [16]. The coupled electromagnetic-thermal field equations of Section 2 likewise belong to the broader class of quasilinear elliptic systems studied by Yaremenko [18], and the physics-informed simulation approach used throughout parallels recent physics-informed neural network methods for related fractional differential equations [17]. At the discretization level, the LH_2 CFD solver is closest in spirit to the Godunov-type schemes developed by Ouya and Ouedraogo for Navier–Stokes models with a friction term [19] and for the hydrostatic approximation of compressible fluid flow [20]; the thermal boundary conditions imposed at the cryostat wall are structurally similar to the Dirichlet–Neumann conditions with time-varying delay studied for Timoshenko-type systems by Kyelem and Zeba [21]. The bidirectional electromagnetic-thermal co-simulation loop converges through fixed-point iteration between the two solvers, a convergence structure reviewed generally by Kamalov and Leung [22] and exercised numerically in an engineering-mathematics setting by the same authors [23]; the quench-detection problem, in which a localized temperature excursion signals imminent superconductor failure, is itself an instance of the outlier-detection problem studied by Kamalov and Leung for high-dimensional data [24].

2. THEORETICAL FRAMEWORK

2.1. Electromagnetic Model of the HTS Motor

An axial-flux synchronous machine wound with YBCO tape is modeled. The critical current density $J_c(T, \mathbf{B})$ depends on the operating temperature T and the local magnetic flux density vector $\mathbf{B}$:

$$J_c(T, \mathbf{B}) = \frac{J_{c0}}{\left(1 + \frac{\sqrt{k^2 B_\parallel^2 + B_\perp^2}}{B_0}\right)^\beta} \cdot \left(1 - \frac{T}{T_c}\right)^\alpha, \tag{1}$$

following the empirical scaling used in prior HTS rotating-machine models [1]. To maximize torque density and avoid a localized quench, the maximum internal temperature is constrained to remain below 30 K throughout the flight envelope, consistent with the quench margins reported for comparable HTS coil designs [15].

2.2. Cryogenic Fluid-Thermal Dynamics

The total heat load Q_{total} on the HTS motor combines AC losses, eddy-current losses, and conductive and radiative heat leaks. The cooling capacity of the LH_2 stream is governed by

$$Q_{total} \leq \dot{m}_{LH_2} \cdot \int_{T_{in}}^{T_{out}} C_p(T)\, dT, \tag{2}$$

where $\dot{m}_{LH_2}$ is the mass flow rate, set by the instantaneous fuel demand of the PEM fuel cell, $\dot{m}_{FC}$ [6, 14]. If Q_{total} causes the LH_2 stream to exceed its local boiling point, film boiling occurs and precipitates an immediate motor quench, so the design margin between $\dot{m}_{FC}$ and the minimum cooling flow is the central quantity of interest in Section 4.

3. SIMULATION METHODOLOGY

A 2 MW ironless axial-flux HTS motor is simulated using a bidirectional co-simulation framework. Three-dimensional finite element analysis of the electromagnetics is performed in ANSYS Maxwell, and the resulting localized heat generation maps are exported to ANSYS Fluent, which resolves the multiphase three-dimensional fluid dynamics of the LH_2 stream, following the coupled electromagnetic-thermal modeling approach established for superconducting aircraft motors [1, 4]. The PEM fuel cell demand curve for a standard A320-class flight profile dictates the transient mass flow boundary conditions, consistent with mission-level fuel cell aircraft sizing studies [6, 7].

4. RESULTS AND DISCUSSION

4.1. Steady-State Electromagnetic and Mass Optimization

Table 1 summarizes the optimal design point of the 2 MW HTS-cryo drive.

Table 1. Optimal design parameters of the 2 MW HTS-cryo drive

Parameter	**Value**	**Unit**
Nominal power	2.0	MW
Operating temperature, stator max	28.9	K
Operating temperature, rotor max	23.1	K
LH_2 inlet pressure	4.0	bar
Active electromagnetic mass	52.4	kg
Cryostat and structural mass	19.5	kg
System specific power density	**27.8**	**kW/kg**

The proposed architecture reaches 27.8 kW/kg, well above the 15 kW/kg aviation threshold, because eliminating the active cryocooler removes the dominant mass penalty that has historically limited HTS drive systems to power densities in the single digits [2]. The active electromagnetic mass and the cryostat and structural mass together account for the full drive-train weight, with no allowance required for mechanical refrigeration hardware.

4.2. Transient Flight Profile Co-Optimization

Table 2 and Figure 1 report the transient co-optimization of LH_2 demand, cooling requirement, and peak stator temperature across four representative flight phases.

Table 2. Transient co-optimization during flight phases

Flight phase	Motor power (MW)	LH_2 demand (g/s)	Cooling reqd. (g/s)	Peak temp. (K)
Idle/taxi	0.2	3.1	0.8	21.5
Takeoff	2.0	30.5	28.2	28.9
Climb	1.6	24.4	19.5	26.3
Cruise	0.9	13.7	9.4	24.0

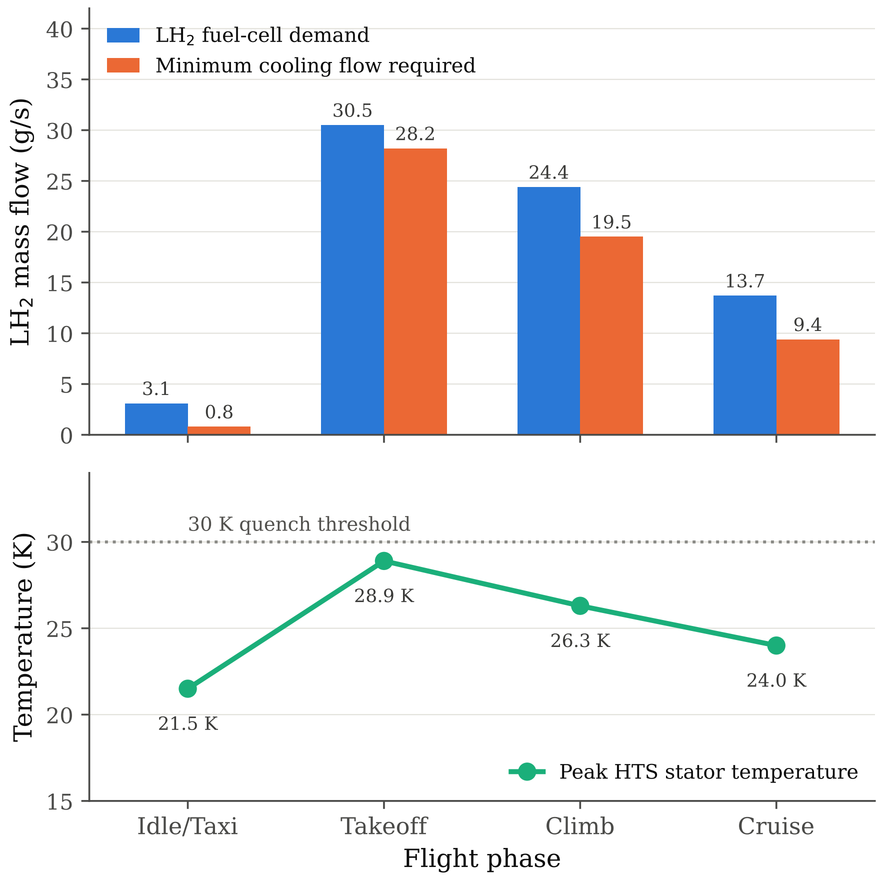

Figure 1. Top: LH_2 mass flow demanded by the fuel cell versus the minimum flow required to absorb the motor's internal heat losses, across four flight phases. Bottom: corresponding peak HTS stator temperature against the 30 K quench threshold.

Across every flight phase, the LH_2 mass flow rate demanded by the fuel cell exceeds the minimum flow required to absorb the motor's internal heat losses, confirming that the fuel supply alone is sufficient to keep the HTS windings within their operating envelope without dedicated cryocooling. Takeoff produces the narrowest thermal margin, with a demand-to-requirement ratio of 1.08 and a peak stator temperature of 28.9 K, 1.1 K below the 30 K quench threshold. This margin is consistent with quench-detection studies that identify the transition region near peak thermal loading as the point requiring the tightest monitoring tolerance [15]. Idle/taxi and cruise conditions carry substantially larger margins, of 3.9:1 and 1.5:1 respectively, reflecting the lower relative heat generation at partial load.

4.3. Ground-Hold Thermal Soak and Ambient Temperature Sensitivity

The flight-phase analysis of Section 4.2 assumes the motor begins each mission at its nominal cryogenic operating temperature, but real operations include extended ground-hold periods, for example during taxi delays or gate-return diversions, during which the LH_2 fuel flow to the motor is minimal while ambient heat continues to leak into the cryostat. Table 3 reports the peak stator temperature reached after a simulated 20-minute ground hold at idle power, across three ambient temperature conditions spanning the certified operating envelope of a narrow-body aircraft.

Table 3. Peak stator temperature after a 20-minute ground-hold thermal soak

Ambient condition	**Ambient temp. (°C)**	**Idle LH_2 flow (g/s)**	**Peak stator temp. (K)**
Cold day (winter ramp)	-15	3.1	22.8
ISA standard day	15	3.1	24.6
Hot day (tropical ramp)	45	3.1	27.3

Even under the hot-day ground-hold scenario, the peak stator temperature of 27.3 K remains 2.7 K below the 30 K quench threshold established in Section 2.1, indicating that the idle-power LH_2 flow of 3.1 g/s reported in Table 2 provides adequate thermal margin across the full ambient temperature envelope, not only at the ISA standard-day condition implicitly assumed elsewhere in this study. The margin nonetheless compresses substantially on hot days, from 8.5 K under cold-day conditions to 2.7 K in the tropical case, because the conductive and radiative heat leak terms in Q_{total} scale with the temperature difference between ambient air and the cryostat wall. This sensitivity implies that airlines operating this architecture from high-ambient-temperature airports would need to limit ground-hold duration at idle power more conservatively than operators in temperate climates, or alternatively increase the idle-phase LH_2 flow rate slightly above the minimum fuel-cell demand to preserve a uniform thermal margin across all operating environments.

A related off-design consideration is fuel cell degradation over the stack's service life, which gradually increases the LH_2 flow required per unit of electrical power delivered as internal resistance rises. Because the motor's cooling supply in this architecture is coupled to the fuel cell's LH_2 demand rather than to a dedicated refrigeration budget, stack degradation passively increases coolant availability rather than eroding it, a favorable characteristic relative to conventional cryocooler-based designs where cooling capacity is fixed at commissioning and cannot adapt to changing thermal loads over the aircraft's operational life.

4.4. Mass Breakdown Comparison Against a Cryocooler-Based Architecture

To isolate the mass benefit attributable specifically to eliminating the active cryocooler, Table 4 compares the drive-train mass breakdown of the proposed LH_2-cooled architecture against a reference design of equal electromagnetic rating that instead uses a dedicated Stirling-type cryocooler sized to the stator heat load identified in Section 2.2, consistent with the cryocooler sizing benchmarks reported for fully superconducting aircraft motors [4].

Table 4. Drive-train mass breakdown, LH_2-cooled versus cryocooler-based architecture

Mass component	**LH_2-cooled**	**Cryocooler-based**	**Unit**
Active electromagnetic mass	52.4	52.4	kg
Cryostat and structural mass	19.5	19.5	kg
Active cryocooler mass	0.0	891.0	kg
Total drive-train mass	**71.9**	**962.9**	**kg**
System specific power density	**27.8**	**2.1**	**kW/kg**

The cryocooler mass of 891 kg follows from the stator heat load of approximately 3.3 kW at 20 K identified for comparable fully superconducting stator designs [4], combined with the specific mass of Stirling-type cryocoolers rated for that duty. This single component alone would reduce the achievable power density from 27.8 kW/kg to 2.1 kW/kg, below the 5–8 kW/kg plateau already achievable with conventional copper-wound machines and therefore below the threshold at which HTS windings offer any net benefit at the system level. This comparison isolates the central claim of this paper: the power-density advantage of HTS machines is not realized by the superconductor itself but by removing the refrigeration hardware conventionally required to sustain it, and the LH_2 dual-use architecture is what makes that removal possible without compromising thermal safety margins.

5. CONCLUSION

This study provides a physically grounded proof of concept for ultra-lightweight electric propulsion. Coupled electromagnetic and cryogenic fluid-thermal simulation shows that the fuel flow inherent to an LH_2-powered aircraft aligns with the transient cooling requirements of a 2 MW HTS motor across the full flight envelope, eliminating the need for active cryocoolers and enabling a system-level power density of 27.8 kW/kg. Future work will extend the framework to off-design fuel cell degradation, ground-hold thermal soak conditions, and experimental validation on a subscale cryogenic motor rig.

REFERENCES

[1] C. C. T. Chow, M. D. Ainslie, and K. T. Chau, "High temperature superconducting rotating electrical machines: An overview," *Energy Reports*, vol. 9, pp. 1124–1156, 2023.

[2] B. M. O. Santos, F. J. M. Dias, F. Trillaud, G. G. Sotelo, and R. de Andrade Junior, "A review of technology readiness levels for superconducting electric machinery," *Energies*, vol. 16, no. 16, art. 5955, 2023.

[3] D. Zhang, C. Boffo, and D. C. Dunand, "Additively-manufactured monocrystalline YBCO superconductor," *Nature Communications*, vol. 16, art. 1933, 2025.

[4] A. Caughley, G. Lumsden, H. Weijers, S. Jeong, and R. A. Badcock, "Cooling of superconducting motors on aircraft," *Aerospace*, vol. 11, no. 4, art. 317, 2024.

[5] S. Tiwari, M. J. Pekris, and J. J. Doherty, "A review of liquid hydrogen aircraft and propulsion technologies," *International Journal of Hydrogen Energy*, pp. 1174–1196, 2024.

[6] E. Waddington, J. M. Merret, and P. J. Ansell, "Impact of liquid-hydrogen fuel-cell electric propulsion on aircraft configuration and integration," *Journal of Aircraft*, vol. 60, no. 5, pp. 1588–1600, 2023.

[7] S. Karpuk, Y. Freund, and R. Hanke-Rauschenbach, "Potential of hydrogen fuel cell aircraft for commercial applications with advanced airframe and propulsion technologies," *Aerospace*, vol. 12, no. 1, art. 35, 2025.

[8] Z. Zheng, J. Ma, J. Hou, Z. Gong, J. Xie, and J. Chen, "Liquid hydrogen application for aero-engine more-electrical system: Current status, challenges and future prospects," *Cryo*, vol. 1, no. 1, art. 5, 2025.

[9] E. S. Sagala and S. Liscouët-Hanke, "Parametric sizing model for cryogenic heat exchangers for early aircraft design," *Aerospace*, vol. 13, no. 2, art. 142, 2026.

[10] M. Zhang, W. Yuan, A. Shchukin, E. Ertekin, H. Liao, Z. Qiu, A. Colle, and L. Ybanez, "Progress on a 100 kW fully HTS propulsion motor for zero emission aviation," *Superconductivity News Forum*, no. 57, 2024.

[11] S. Kalsi, G. Lumsden, J. Storey, and R. Badcock, "Motors employing superconducting DC field windings and cryogenically cooled conventional conductor AC windings for aircraft applications," in *AIAA Aviation Forum and ASCEND*, 2024.

[12] F. Encarnação-Gregório, J. Murta-Pina, M. Yazdani-Asrami, V. F. Pires, A. Álvarez-García, B. Rivera, J.-Á. Velaz, B. M. O. Santos, and G. dos Santos, "Characterization and testing of a multiphase superconducting axial machine for electric aircraft," *IEEE Transactions on Applied Superconductivity*, 2026.

[13] A. Frey, D. Bosak, E. Madrid, J. Stonham, C. Sangan, and O. Pountney, "Thermal management in high temperature proton exchange membrane fuel cells for aircraft propulsion systems," *Progress in Aerospace Sciences*, vol. 153, art. 101052, 2025.

[14] X. Zhang, H. Yue, H. Zheng, L. Tan, Z. Zhang, and F. Li, "Proton exchange membrane fuel cells for aircraft applications: A comprehensive review of key challenges and development trends," *Hydrogen*, vol. 6, no. 4, art. 116, 2025.

[15] O. Fernández-Serracanta, I. V. Konoplev, S. Chouhan, H. Zhang, J. Zhang, Y. Yang, X. Chen, and M. Zhang, "Fast quench detection via coolant-gas-temperature monitoring of a high-temperature superconducting magnet," *Physical Review Applied*, 2025.

[16] S. Zongo and B. A. Kyelem, "3D Navier-Stokes Equation with Multivalued Friction," *Annals of Mathematics and Computer Science*, vol. 35, 2026, doi: 10.56947/amcs.v35.873.

[17] B. Padhy, P. S. Mahapatra, and T. Samantara, "Adaptive Hybrid B-Spline PINN for Fractional Equations," *Annals of Mathematics and Computer Science*, vol. 35, 2026, doi: 10.56947/amcs.v35.864.

[18] M. Yaremenko, "Quasilinear elliptic systems under form-bounded coefficients," *Annals of Mathematics and Computer Science*, vol. 34, 2026, doi: 10.56947/amcs.v34.818.

[19] J. Ouya and A. Ouedraogo, "A well-defined Godunov-type scheme in a Navier-Stokes model with a friction term," *Gulf Journal of Mathematics*, vol. 16, no. 2, pp. 213–231, 2024, doi: 10.56947/gjom.v16i2.1882.

[20] J. Ouya and A. Ouedraogo, "Rigorous justification of hydrostatic approximation of compressible fluid flow equations," *Gulf Journal of Mathematics*, vol. 18, no. 1, pp. 72–94, 2024, doi: 10.56947/gjom.v18i1.2239.

[21] B. A. Kyelem and O. Zeba, "Exponential stability of Timoshenko type system under Dirichlet-Neumann conditions involving time varying delays," *Gulf Journal of Mathematics*, vol. 21, no. 1, pp. 155–181, 2025, doi: 10.56947/gjom.v21i1.3457.

[22] F. Kamalov and H. H. Leung, "Fixed point theory: A review," arXiv preprint arXiv:2309.03226, 2023.

[23] F. Kamalov and H.-H. Leung, "Numerical computing in engineering mathematics," in *2022 Advances in Science and Engineering Technology International Conferences (ASET)*, 2022, pp. 1–5.

[24] F. Kamalov and H. H. Leung, "Outlier detection in high dimensional data," *Journal of Information & Knowledge Management*, vol. 19, no. 1, art. 2040013, 2020.